



# Use of Sentinel-2 images for the detection of precursory motions before landslide failures

Pascal Lacroix<sup>a,\*</sup>, Grégory Bièvre<sup>a</sup>, Erwan Pathier<sup>a</sup>, Ulrich Kniess<sup>b</sup>, Denis Jongmans<sup>a</sup>

<sup>a</sup> Univ. Grenoble Alpes, Univ. Savoie Mont Blanc, CNRS, IRD, IFSTTAR, ISTerre, Grenoble F-38000, France

<sup>b</sup> von Lieberman GmbH, Ruhrstrasse 57, Hamburg 22761, Germany

## ARTICLE INFO

### Keywords:

Landslides  
Precursors  
Sentinel-2  
Optical satellite  
Medium resolution

## ABSTRACT

The Sentinel-2 optical satellites provide a global coverage of land surfaces with a 5-day revisit time at the Equator. We investigate the ability of these freely available optical images to detect precursory motions before rapid landslides. A 9-month time-series of displacement is derived from Sentinel-2 data over a major landslide in the French Alps, which exhibited a sudden reactivation in June 2016. This analysis reveals a 7-month period of low activity ( $\leq 1$  m), followed by a sudden acceleration of  $3.2 \pm 1.2$  m in 3 days, before the failure of a mass of about  $2$  to  $3.6 \cdot 10^6$  m<sup>3</sup>. The location of this precursory motion is consistent with that of the slow motions occurring since 2001 (about 1 m/year), as revealed by aerial photographs and LiDAR analysis. This change in activity over a very short period of time (days) emphasizes the value of the frequent revisit time of Sentinel-2, despite its medium resolution of 10 m. We finally simulate the ability of Sentinel-2 for detecting these precursory patterns before a rapid landslide occurs, based on typical Voight's laws for creeping materials, characterized by a power law exponent  $\alpha$ . Based on this analysis and on global cloud cover maps, we compute the probability to detect pre-failure motions of landslides using the Sentinel-2 constellation. This probability is highly heterogeneous at the global scale, affected by the revisit time of the satellite and the cloud cover. However the main factors controlling this detection ability are the properties of the landslide itself (its size and the  $\alpha$  parameter), with almost 100% of detection probability for  $\alpha = 1.3$  and 0% for  $\alpha = 1.8$ . Despite all these limitations, probability to detect a motion before a landslide failure often reaches 50% for classical landslide parameters. These results open new perspectives for the early warning of large landslide motion from global and open source remote sensing data.

## 1. Introduction

Slow-moving landslides are mass movements with velocities ranging from a few cm/year to a few m/year (Hung et al., 2014). Their dynamics can be controlled by rainfall (e.g. Iverson, 2000), earthquakes (e.g. Lacroix et al., 2014), or fluvial erosion (e.g. Zerathe et al., 2016). They may exhibit sudden accelerations or failures that can evolve toward catastrophic flows (Jongmans et al., 2009; Van Asch et al., 2009), posing a threat to infrastructures and local populations. This was dramatically illustrated in the Vajont landslide in 1963, where slow motions of a few cm/days were observed during the 3 years prior to a catastrophic collapse that caused 1900 casualties (Hendron and Patton, 1985). In this context, monitoring slow motions is key for detecting precursors for major landslides.

Many observations report slow motions with patterns showing an accelerating displacement rate before landslide failure (Bhandari, 1988; Zvelebil and Moser, 2001; Petley et al., 2002; Federico et al., 2012).

This pre-failure phase can also be revealed by increasing seismic release rate in brittle materials (Amitrano et al., 2005) or seismic velocity variations in ductile materials (Mainsant et al., 2012a,b). These patterns can be explained in brittle materials by the initiation and progressive maturation of rupture surfaces through subcritical crack growth (Lacroix and Amitrano, 2013), and/or by the progressive loss of the material elastic properties, caused by water content increase or overloading in ductile materials (Mainsant et al., 2012b).

Precursory motions have been regularly observed in ground displacement data acquired on instrumented landslides (e.g. Federico et al., 2012, for a review). The acceleration is found to follow either an exponential (Petley et al., 2002) or a power law (e.g. Fukuzono, 1985; Voight, 1989) toward the time of the collapse. Such laws have been proposed as a tool for determining the time of collapse (Federico et al., 2012).

Monitoring slow movements over a wide area from space is then a key issue in landslide risk management. Very few studies have however

\* Corresponding author.

E-mail address: [pascal.lacroix@univ-grenoble-alpes.fr](mailto:pascal.lacroix@univ-grenoble-alpes.fr) (P. Lacroix).

used remote sensing data to detect acceleration precursor to a slope failure. Both Interferometric Synthetic Aperture Radar (InSAR) (Hilley et al., 2004; Calabro et al., 2010; Kos et al., 2016; Dong et al., 2018; Intrieri et al., 2018) and optical image correlation techniques (Delacourt et al., 2004; Debella-Gilo and Kaab, 2012; Stumpf et al., 2014; Lacroix et al., 2015; Stumpf et al., 2017) have been widely used to detect and measure motions over slow-moving landslides. Time-series of displacement have been sometimes generated to document the pre-failure motion of landslides. For instance, Sun et al. (2015) applied Interferometric Synthetic Aperture Radar (InSAR) data to document the pre-failure motion of the Zhouqu landslide. They detected centimetric scale motions, which do not however fully coincide with the location of the catastrophic flow. Kos et al. (2016) used InSAR data on the Moosfluh landslide in Switzerland to monitor its activity over 20 years, and show a progressive acceleration of the movement associated with multiple failure events of increasing size with time. Two recent studies have shown the ability of radar satellites with high revisit-time (Sentinel-1, ALOS-2) to detect an acceleration of a catastrophic landslide in China 12 days before its failure (Dong et al., 2018; Intrieri et al., 2018), highlighting its interest for detecting short transient motions prior to slope failures.

However, the use of InSAR data is still limited to areas with favourable slope orientation, low vegetative cover, and low velocity (few cm/days). Alternatively, the correlation of diachronic optical images allows these limitations to be overcome. The launch of new constellations of satellites with a short revisit time (on the order of a few days) theoretically enables the generation of time-series of displacement (Stumpf et al., 2017). Displacement time-series from optical images have been undertaken over various areas affected by landslides, showing decadal accelerations (Strozzi et al., 2010) or decelerations (Bennett et al., 2016) of mass movements, as well as their seasonal motion (Stumpf et al., 2017) or transient motions due to earthquakes (Lacroix et al., 2015). Those latter studies use very high-resolution satellite images or aerial photographs, preventing their systematic use at a high-frequency rate over a wide area. The launch of new constellations of medium resolution satellites with a frequent repetitive time (8 days for Landsat7/8, 5 days for Sentinel-2 at the Equator), is an opportunity to have access to transient motions of landslides over a few days. The displacement uncertainty obtained with such techniques (typically one-fifth of a pixel size (Stumpf et al., 2014; Lacroix et al., 2015)) is however much larger than for InSAR, which makes it difficult to detect small transient motions prior to landslide failures. Therefore, this technique has never been applied for detection of landslide acceleration precursor to its failure.

This study aims to explore the possibility of detecting the low but significant motions that can precede a landslide, using optical images from the Sentinel-2 satellite characterized by a frequent (5 days at the Equator) revisit time. The chosen event is a major reactivation of the large Harmalière landslide (French Alps) that occurred in late June 2016.

## 2. Study site

The Trièves area in the French Western Alps (Fig. 1a) is a wide depression (300 km<sup>2</sup>) filled with alternations of Quaternary clays and silts deposited in a glacially-dammed lake during the Last Glacial Maximum. In the study area, the sediment thickness varies between 0 m and almost 300 m (Bièvre et al., 2011). After the retreat of the glacier, around 15 000 to 25 000 years ago, rivers started to incise the soft clayey sediments and initiated landsliding in the whole area. Presently, around 15% of the Trièves is estimated to be sliding (Jongmans et al., 2009) at low-velocity rates (few cm/year motions have been measured on the monitored landslides of the area). The Harmalière landslide is located on the western bank of the man-made Lake Monteynard. Its historical activity can be traced back to the late 19th century at least (Moulin and Robert, 2004), where intense gullying and landsliding at

the toe of the slide induced afforestation operations.

The 1450 m-long Harmalière landslide affects an area of around  $1.8 \times 10^6$  m<sup>2</sup> (Fig. 1a). The slope is 15% in the upper part and around 10% in the lower part. This slight slope break in the mid-length of the slide corresponds to a change in the deformation mechanism. According to the classification proposed by Hung et al. (2014), the Harmalière landslide is a compound earthslide in its upper part, showing significant internal deformation with numerous scarps and counter-scarps. Studies using either aerial photographs (Fernandez and Whitworth, 2016) or comparison of Lidar data (Knieß, 2011) show velocities of about 1 m/year in between 2001 and 2009. In its lower part, the landslide evolves into an earthflow and eventually a mudflow (Bièvre et al., 2011).

A very large landslide occurred on March 7 1981, after snowmelt and heavy rainfalls, resulting in the mobilization of a surface of around  $0.45 \times 10^5$  m<sup>2</sup> of clayey material. The volume of clay that entered the lake was estimated to be around  $0.25 \times 10^6$  m<sup>3</sup> (Al Hayari et al., 1990; Giraud et al., 1991). Back analysis suggests that the depth of the deepest shear surface is around 45 m (Al Hayari et al., 1990), which is typical within the Trièves area (Van Genuchten and Van Asch, 1988; Van Asch et al., 2009; Renalier et al., 2010a,b; Bièvre et al., 2012).

This landslide suffered several reactivation phases (Moulin and Robert, 2004), among which the most important ones occurred in January 1988, January 1996 and September 2004. They mainly consisted of regressions of the main headscarp, a typical mechanism of retrogressive landslide in these fine-grained formations (Van Asch et al., 1984). The last major reactivation, studied here, occurred on June 27 2016. Field observations revealed a northward regression of the headscarp over a maximum distance of 30 m. A compact block of clays with an estimated volume of  $2$  to  $3.6 \times 10^6$  m<sup>3</sup> slid along a shear plane. The new headscarp of the landslide presents a 15 to 30 m sub-vertical scarp (Fig. 1b) marked by strias, showing fragile deformation. At the toe of the landslide, up to 10 m of clayey material was accumulated. The deformational pattern of the lower part shows flow-like surface morphology and flank ridges. These patterns reveal ductile deformation, typical of an earthflow.

## 3. Data and methods

### 3.1. Sentinel-2 data

We processed data from the recently launched Sentinel-2A satellite over a selected area of  $4 \times 5$  km<sup>2</sup>. Starting in November 2015, it provides free images with global coverage of land and coastal areas. The Sentinel-2 mission is now a constellation of two satellites, following the launch of the Sentinel-2B satellite in March 2017. The satellite offers a resolution of up to 10 m for blue (B2), green (B3), red (B4) and infra-red (B8) bands. The data were processed for the different bands. The process realized with the different bands provides similar results, showing similar patterns. The differences between results obtained with 2 different bands exhibit standard deviation close to 50 cm, which is about one-third of the measurement uncertainties (see Section 4.1). In this study, results obtained with the blue band B2 are exposed.

The attractive feature of the Sentinel-2 constellation is its frequent revisit time of 5 days at the Equator under cloud-free conditions. The monitored landslide, situated at 45° North, is covered by 2 satellite swaths (Table 1), providing twice more acquisitions than at the Equator. The data, however, have different viewing angles, which affects their orthorectification quality and therefore their comparison (e.g. Lacroix et al., 2013). 22 cloud-free images were available (over 47 total images acquired) between December 7, 2015 and September 2, 2016 (Table 1). Among these images, two of them display thin clouds (March 26, 2016 and May 5, 2016), which however do not prevent from visualizing the ground surface. Therefore, we decided to keep them in our analysis. The Level-1C products provided online by the European Spatial Agency (ESA) Sentinel hub were used. These products are derived using the PlanetDEM90 Digital Elevation Model (DEM) to project

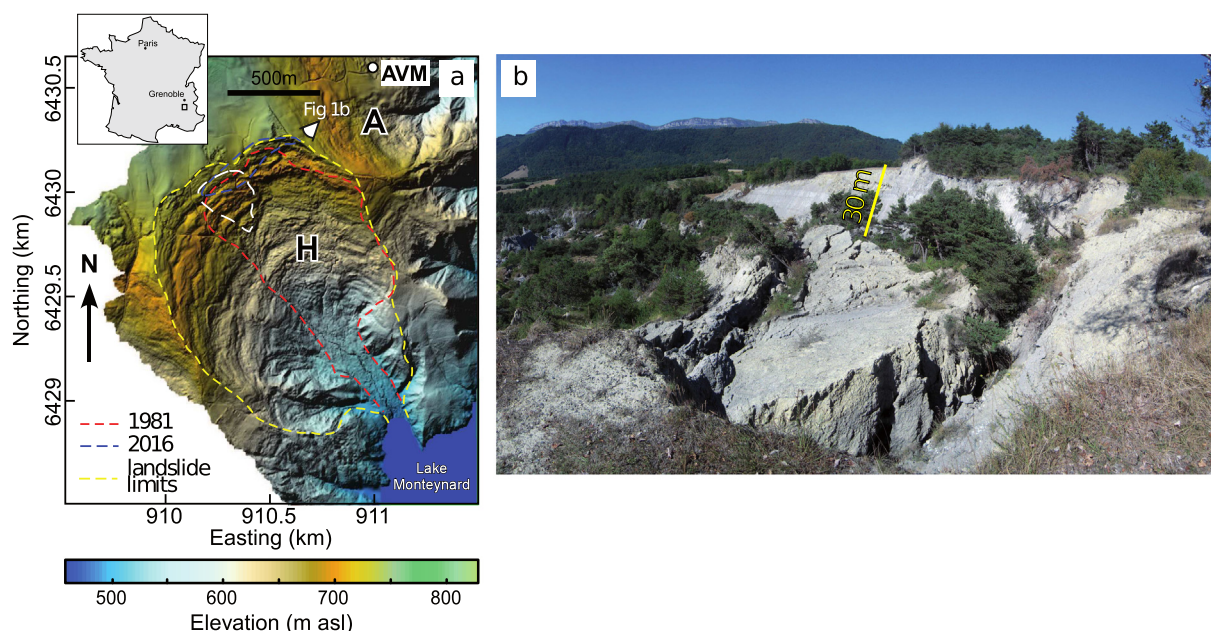


**Fig. 1.** a) Location and morphology of the study site. The topographical map with a color scale is derived from a LiDAR DEM acquired in 2009. A: Avignonet landslide; H: Harmalière landslide. AVM: permanent seismological station of the OMIV Observatory (RESIF, 2006). 1981: surface mobilized by the 1981 earthflow; 2016: headscarps created by sudden regression events; limits of the Harmalière landslide derived from the 2009 LiDAR DEM are shown with a yellow dashed contour. The white contour locates the area of motion detected between 2001 and 2009 (Knieß, 2011; Fernandez and Whitworth, 2016). Coordinate system is Lambert93-RGF93 in m. b) Photo of the June 2016 reactivation (see the photograph location in a). View looking west, showing the sliding mass at the head-scarp. (For interpretation of the references to color in this figure legend, the reader is referred to the web version of this article.)

**Table 1**

Metadata of Sentinel-2 images used in this study.

Orbit #	Dates
R008	30/12/2015 19/03/2016 28/04/2016 28/05/2016 27/06/2016 07/07/2016 17/07/2016 16/08/2016 26/08/2016
R108	07/12/2015 17/12/2015 27/12/2015 26/01/2016 26/03/2016 25/04/2016 05/05/2016 15/05/2016 24/06/2016 03/08/2016 13/08/2016 23/08/2016 02/09/2016

the image into cartographic geometry (Drusch et al., 2012).

Horizontal displacement fields were calculated using the sub-pixel correlation algorithm implemented in Cosi-Corr (Leprince et al., 2007). Successive diachronic images were correlated to produce 21 displacement fields with short time intervals (between 3 and 53 days). This approach was chosen to reduce the decorrelation effect between the images that are located in an area where vegetation and agricultural crops induce rapid changes of the land-cover. The correlation was processed in the spatial domain using a window size of 16 pixels and a search radius of 100 m. The window size was chosen as a compromise between the robustness of large windows and the ability of smaller windows to detect motions of rather small objects (typical size of  $100 \times 100 \text{ m}^2$ , that is  $10 \times 10$  pixel size). The search radius was chosen large enough (100 m or 10 pixels) to detect possible large displacements of the landslide. Displacement vectors were then projected along the local maximum slope direction, obtained from a 1 m resolution Light Detection And Ranging (LiDAR) DEM resampled at 10 m resolution. This change in resolution is required because the landslide roughness can cause the surface slope measured at a high spatial resolution to vary considerably from the local direction of landslide motion (Roering et al., 2009).

### 3.2. Displacement field filtering

The raw displacement fields, obtained with Cosi-Corr, were corrected from possible misalignments, by shifting them along NS and EW

directions by their median value calculated over the stable area (Fig. 2). Finally, the displacement fields were filtered based on 4 criteria: (1) Quality (e.g. Berthier et al., 2005), that is pixels with correlation coefficients below 0.4 are removed from the analysis. (2) Direction of the motion relative to the slope direction, a criterion specific to landslide studies (Stumpf et al., 2014), that is all pixels with a direction of motion different by more than  $60^\circ$  from the local maximum slope direction are removed. (3) Significance, that is pixels with motion below 0.5 m are not considered in the analysis. This value has been chosen relative to the displacement uncertainty (see Section 4.1), to remove points on stable areas or with low motion amplitudes. This criterion does not affect the values themselves, but slightly the uncertainty, increasing the standard deviation on the stable area values by 14% (see Section 4.1). (4) Connectivity, that is only the pixels with at least 40% of non-masked pixels in their direct vicinity were kept. This criterion was applied to remove isolated pixels.

The parameters of the filter were chosen after a sensitivity analysis, in order to significantly reduce the number of false alarms on the stable areas, without impacting the unstable areas. Their choice is however not critical for our study because it does not impact the values of displacement but only acts as a mask.

## 4. Results

### 4.1. Sentinel-2 displacement field uncertainties

The displacement uncertainties of the measurements situated in the stable area and projected onto their local slope direction are calculated for the 21 displacement fields, using the standard deviation over a stable area. A stable area of  $2.2 \text{ km}^2$  (Fig. 2) has been chosen close by the active landslide area, and not covering the lake where large artifacts occur. Fig. 3 shows the computed uncertainty as a function of the time interval between two acquisitions. The mean computed uncertainty is 1.8 m, but there is a large variability between displacement fields (Fig. 3) due to three effects.



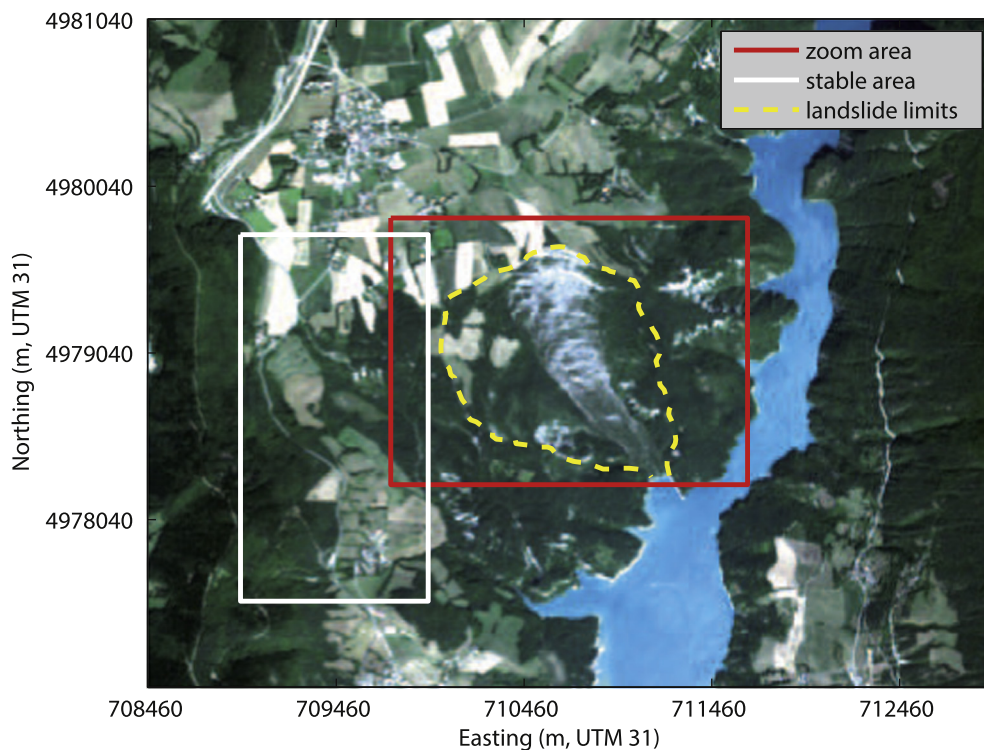


**Fig. 2.** Example of a Sentinel-2 image used in this study (26/08/2016). The red rectangle area represents the footprint of the images shown in Fig. 4. The white rectangle contour defines the stable area where uncertainties were calculated. The yellow dashed line is the landslide limit. (For interpretation of the references to color in this figure legend, the reader is referred to the web version of this article.)

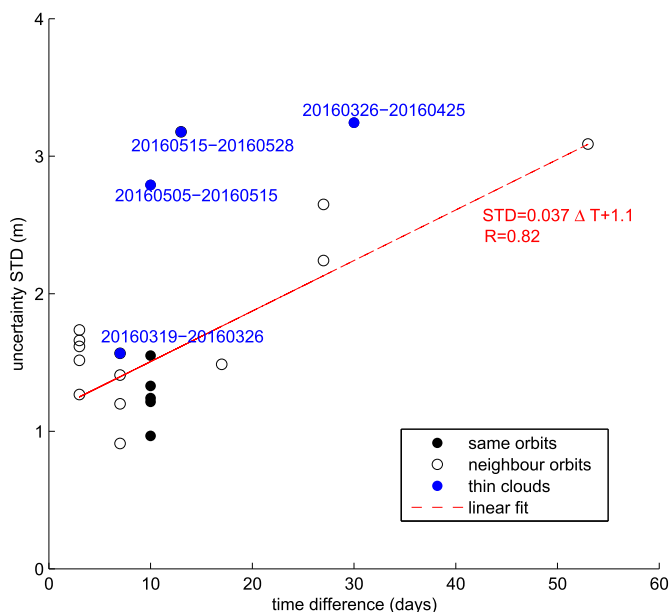


**Fig. 3.** Uncertainties on the slope-projected displacement field represented as a function of the time interval between the 2 acquisitions. The linear fit is computed for the data without clouds (white and black points).

- First, large errors are found for 4 displacements fields presenting thin cloud cover (see Fig. 3), that is where the ground is still observable through clouds but these alter the image dynamics and thus the correlation quality. If we remove those points from our analysis, the mean uncertainty decreases to 1.59 m. This shows that the image choice is important for the displacement time-series generation.
- Second, we notice an increase in the uncertainty with the time interval between two acquisitions (See the linear fit for the data without any clouds in Fig. 3), resulting from the time decorrelation between successive acquisitions. This justifies computing

displacement fields between images with the smallest time interval as possible to reduce uncertainties and detect changes over a short time-period. However, for very slow landslides, short time baselines can limit the motion detection. The strategy to derive the time-series must then be adapted by taking into account also longer time baselines. A promising approach to generate robust time-series at both short and long time steps would be the short baseline techniques developed for InSAR studies (e.g. Berardino et al., 2002), where interferograms are performed between optimal pairs of images, with limited perpendicular and temporal baselines to reduce the noise. Recent studies show the interest of these techniques to generate displacement time-series also from optical images (Bontemps et al., in press).

- Third, excluding the acquisition with cloud cover, the displacement fields between acquisitions with the same orbit (separated by a multiple of 10 days) have lower uncertainties (1.26 m on average against 1.73 m when considering different orbits). This shows the effect of the orthorectification quality. Indeed, errors of the DEM affect similarly images with the same viewing angles, and thus vanish when comparing them together (Altena and Kaab, 2017; Kaab et al., 2016). For images from two neighbour orbits, the difference between the viewing angles is  $6^\circ$  ( $B/H = 0.2$ , see Lacroix et al., 2013), which increases orthorectification uncertainties on areas with low DEM quality (mostly on steep slopes).

#### 4.2. Displacement history

In the time period 2001–2009, the landslide motion history is constrained by Lidar data and aerial photographs (Knieß, 2011; Fernandez and Whitworth, 2016), which show displacements on the order of 1 m/year on the upper part of the Harmalière landslide (Fig. 1). Between 2009 and 2015, there were no motion measurements. The comparison of the morphology between 2009 and 2015 does not show any detectable landslide reactivation.

Between December 7 2015 and June 24 2016, the Sentinel-2 images did not detect any significant motion coherent in space and time (Fig. 4a). All the detected motions during this time period are within

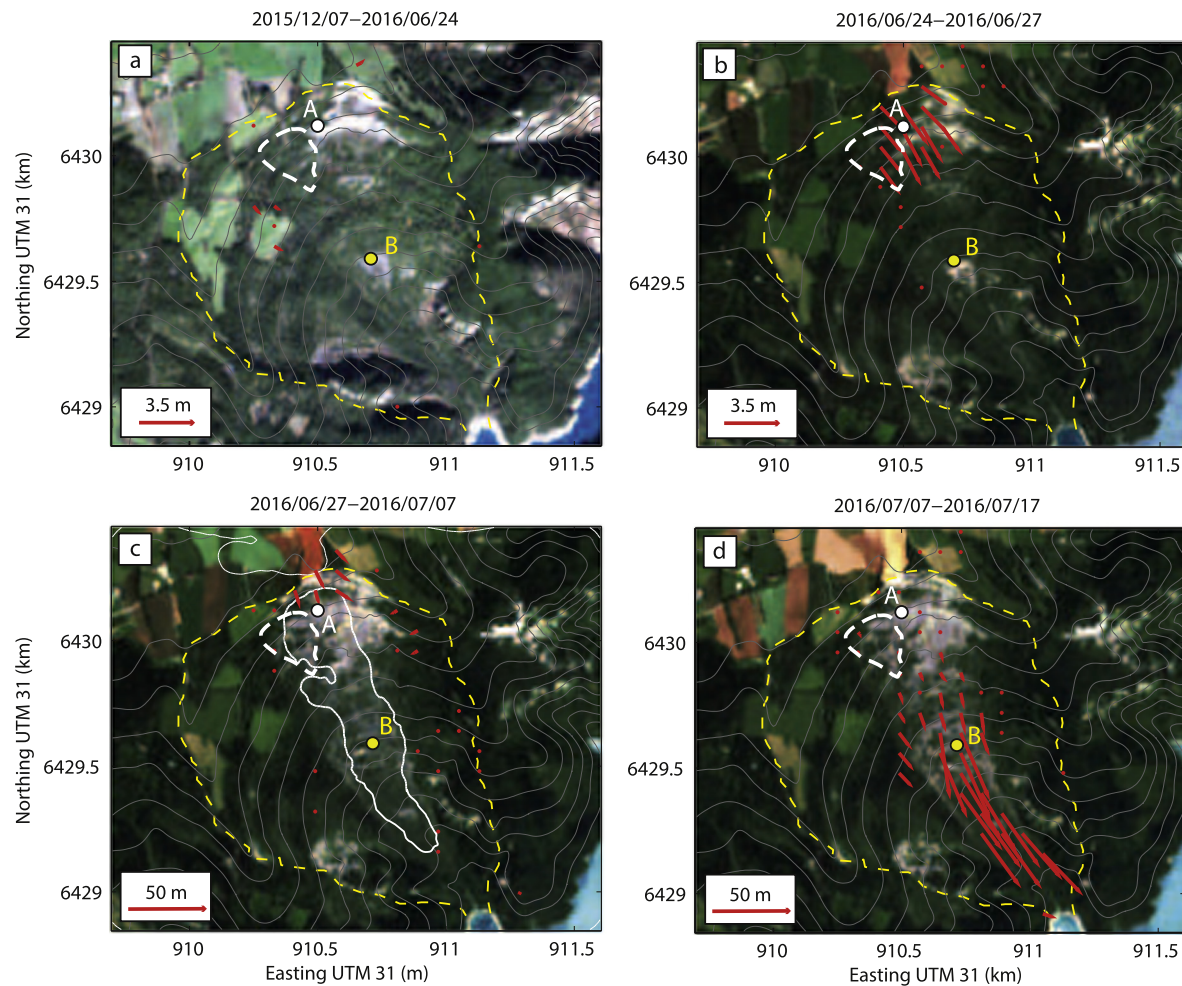


**Fig. 4.** Series of displacement fields calculated using diachronic Sentinel-2 images (color composition of B2, B3 and B4 bands) overlaid over the second image of each pair: a) for the 2015/12/07–2016/06/24 period, b) for the 2016/06/24–2016/06/27 period, c) for the 2016/06/27–2016/07/07 period, when the major reactivation occurred on top of the landslide, and d) for the 2016/07/07–2016/07/17 period. The area where decorrelation occurs is contoured with a white line on the subplot c. The white dashed line represents the mass sliding with a velocity of about 1 m/year from 2001 to 2009. The landslide limits are contoured with a dashed yellow line. The white and yellow points, denoted as A and B, locate the two sites where the time-series are drawn (Fig. 5A and B). Elevation contour lines are spaced every 20 m. Velocity vectors are represented every 8 pixels for better clarity. (For interpretation of the references to color in this figure legend, the reader is referred to the web version of this article.)

the uncertainty (Fig. 5).

The displacement field derived from Sentinel-2 images between June 24 and 27 10h40 UTC, shows a clear movement in the slope direction at the headscarp (N170) (Fig. 4b). This motion of  $3.2 \pm 1.2$  m in 3 days (Fig. 4a), is coherent in space and much higher than the displacement uncertainty. The location of this moving mass is consistent with the subsequent landslide (Fig. 4c), showing a pre-event acceleration. Fig. 5A shows the velocity time-series for a point A, located on this moving upper mass. In the period June 27 2016–July 7 2016, the upper part of this sliding mass was still active with about 14 m of displacement over 10 days (Fig. 4c). In the same time-period, the image analysis shows that the lower part of this mass collapsed.

The image analysis reveals a major landslide event between June 27 2016 and July 7 2016 (Fig. 4c). This failure leads to a complete change of the morphology and the ground-cover on the underneath slope. As a consequence, image decorrelation prevents estimating the displacement field in this area during this time-period (Fig. 4c). The failed mass encompasses the area sliding since 2001 but is even larger (Fig. 4b). Testimonies from local inhabitants indicated that the main landslide was initiated on June 27th between 12 h and 13 h UTC, that is about 2 h after the satellite image acquisition.

After July 7, we observe a fast motion of the flowing material in the

lower part of the slope toward the lake (Fig. 4d). Maximum calculated peak velocities are 5.9 m/day between July 7 and July 17. Fig. 5B shows the velocity time-series for a point B, located in the middle part of the slope. At this point, the velocity reaches a peak of 5.2 m/day in the 20 days following the main failure (Fig. 5B), and then decreases rapidly in about 1 month. At the bottom of the slope, the motion attenuation is slower, and the stability is reached at the beginning of September, showing a two-month attenuation of the material flow. After July 17, the upper block is stable, or at least exhibits a motion lower than the displacement uncertainty (Fig. 5A).

## 5. Discussion

### 5.1. The Harmalière landslide case study

Observations suggest that limited areas located in the upper part of the Harmalière landslide moved with a velocity of about 1 m/year over 15 years (2001–2016). From 24th June 2016, the displacements in a larger upper part of the earthslide suddenly increased to 3.2 m in 3 days, followed by the main failure on 27th June 2016 (Fig. 5A). This slid mass covers an area of around  $8 \times 10^4$  m<sup>2</sup> at the headscarp, as evaluated from field observations conducted in early July 2016 and

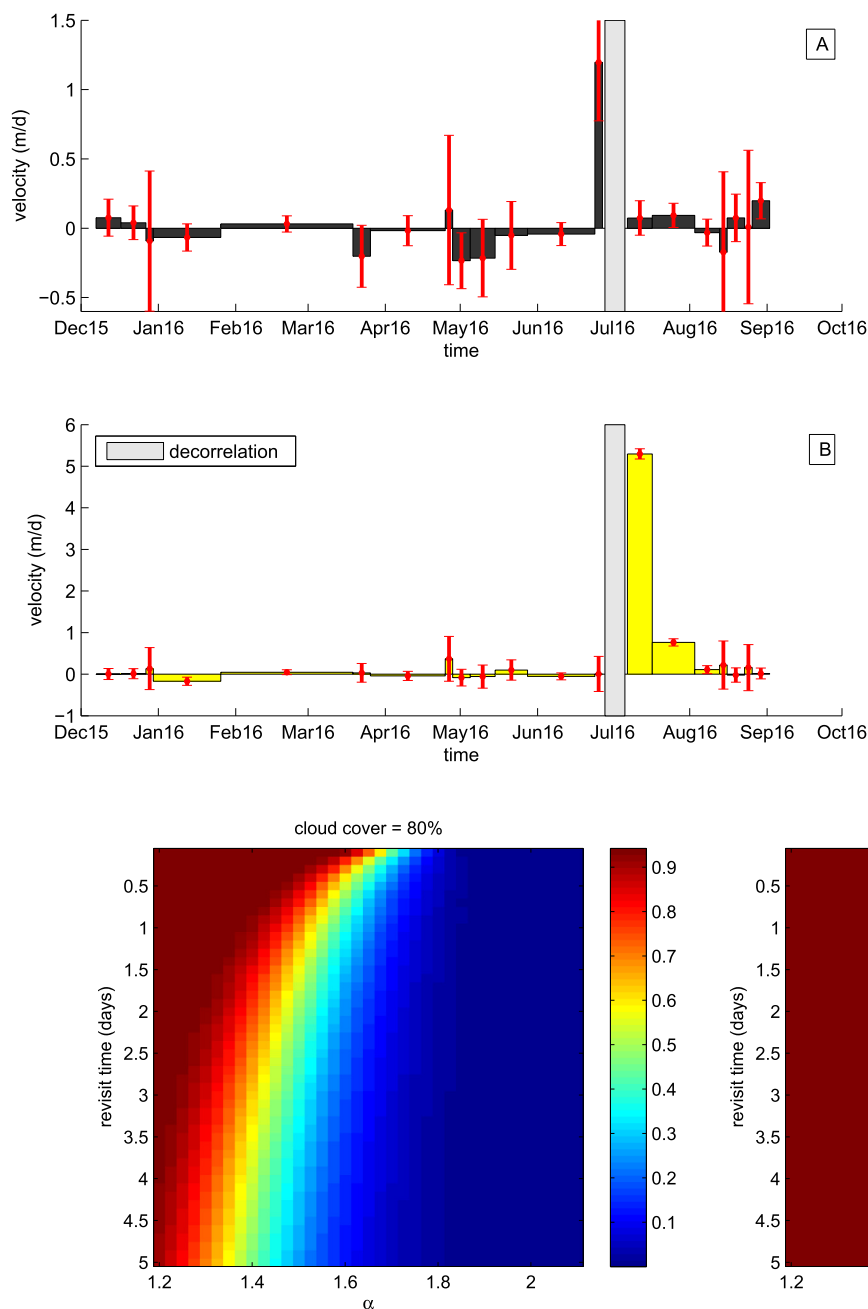


**Fig. 5.** Time-series of slide velocity (m/day) calculated in the slope direction (downward is positive) at the 2 points labelled A and B in Fig. 4: (A) point A is situated on the upper soil mass, just beneath the 2016 headscarp, (B) point B is situated in the middle of the slope. The grey bar indicates the failure time when large morphological changes caused image decorrelation. Velocity error bars are shown in red. (For interpretation of the references to color in this figure legend, the reader is referred to the web version of this article.)

**Fig. 6.** Probability that Sentinel-2 data can detect a pattern of movement precursor of a landslide failure as a function of the satellite revisit time, for a varying landslide characteristic  $\alpha$  and  $A = 0.052$  (see text for details), and for two cloud cover probabilities (left is for 80%, right for 20%).

from Sentinel-2 images. Using the back-analyzed value of 45 m for the depth to the deepest shear surface in these clayey formations (Al Hayari et al., 1990) leads to a maximum volume estimate of around  $3.6 \times 10^6 \text{ m}^3$ . The near-vertical headscarp of up to 30 m also favours the hypothesis of such deep shear surface. This sliding mass supplied an earthflow downslope, which was activated within 10 days after the main failure. The flow slowly attenuated over 2 months to reach stability in September 2016 (Fig. 5B). The velocity time series derived from satellite images bring valuable insight into the landslide kinematics, showing highly transient motions and a fast evolution of the landslide toward the failure. This rapid evolution toward the failure highlights the difficulty to anticipate the failure time of the sliding mass. It also shows the very high value of satellites with frequent revisit time to monitor landslide activity and to detect transient motions. In this case-study, metric precursory motions were observed a few days

before the failure.

The observed motion is theoretically only horizontal as image correlation of perfectly orthorectified images leads to motions in the horizontal plane. However, the images are certainly not perfectly orthorectified as indicated by increasing uncertainties when comparing images of neighbour orbits. Altena and Kaab (2017) and Kaab et al. (2016) showed that orthorectification errors have 2 origins. First, for correlation of neighbour orbit images, errors arise from orthorectification bias due to DEM errors. Second, for repeat-track and neighbour orbits, possible changes of surface elevation between the 2 passes (due to active processes) also lead to orthorectification errors and thus to horizontal errors in the correlation. On the Harmalière landslide, the observed motion is oriented almost completely in the along track direction so that the first type of errors reduced a lot. Indeed, the difference in angle between the flight direction and the flow direction is



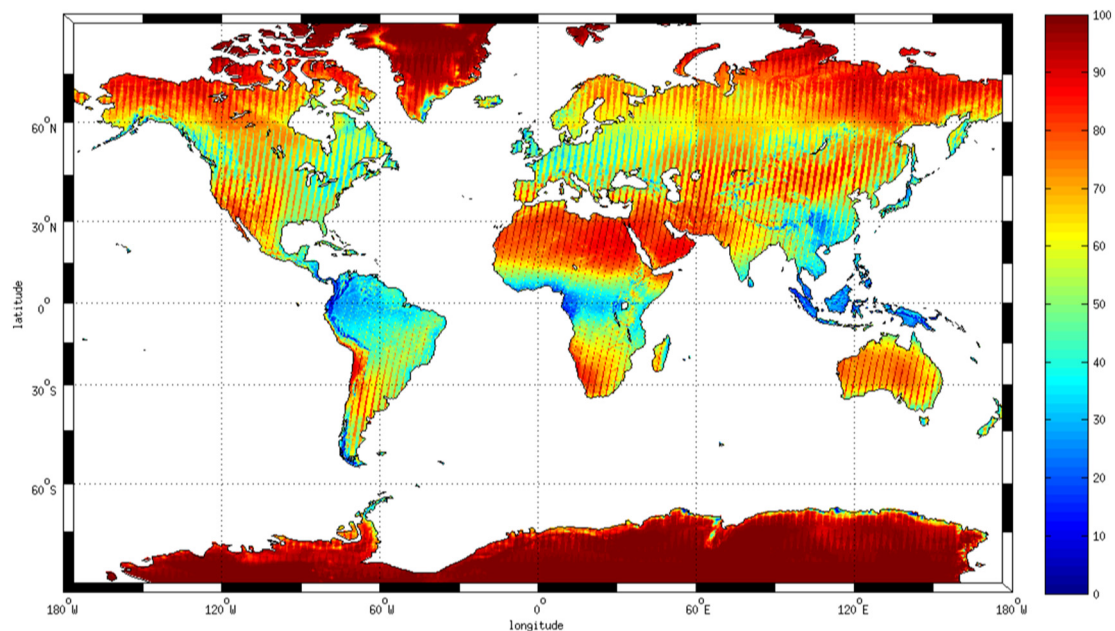


**Fig. 7.** Global map of probability (in %) that Sentinel-2 constellation can detect a pattern of movement precursor of the failure, for landslide characteristics  $\alpha = 1.5$  and  $A = 0.052$ .

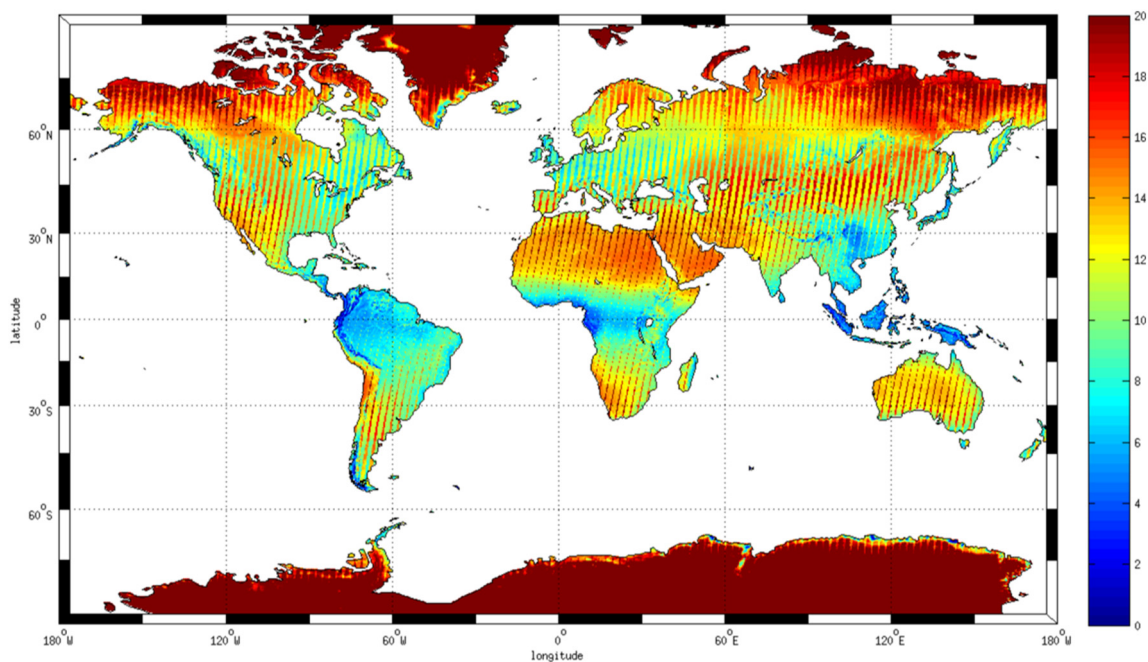


**Fig. 8.** Global map of probability (in %) that Sentinel-2 constellation can detect a pattern of movement precursor of the failure, for landslide characteristics  $\alpha = 1.7$  and  $A = 0.052$ .

15 degrees at the headscarp where the precursory motion was measured. The second source of errors can originate from possible vertical motions of the landslide between the 2 passes. This second type of error can exist in the flow, where transport of sediments can lead to elevation variations. It can also occur at the headscarp, where near-vertical faults suggest that the slow motion is far from perfectly horizontal. Therefore a part of the detected precursory motion is vertical, which is in a good agreement with fields observations (Fig. 1). The sensitivity of the satellite to the vertical motion is increased by using images of neighbour tracks. This analysis should drive the way the time-series are generated for monitoring of landslide headscarps, where motions are often more vertical than in the accumulation area.

A second minor reactivation occurred on 11 and 12 November 2016. No precursory motions were detected using Sentinel-2 data, due to the small surface area of the reactivated mass (about 200 m<sup>2</sup>, that is 2 pixels). Even non-cloudy pre- (1 November) and post- (12 December) failure images comparison does not show discernible differences in morphology. This highlights that small landslides can not be detected with Sentinel-2, because of the medium resolution of the satellite images (10 m). This size limitation is key for landslide detection and more case-studies are needed to quantify the landslide-size limit for detection.

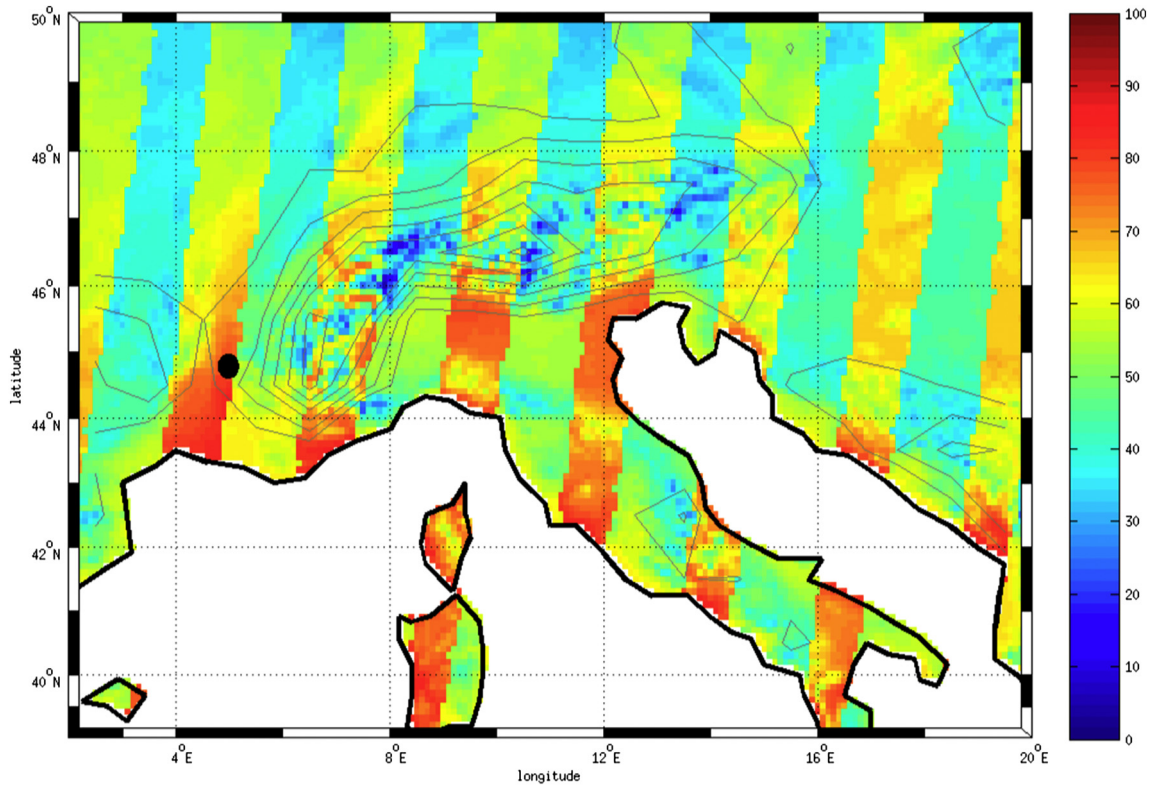


Fig. 9. Map of probability (in %) that Sentinel-2 constellation can detect a pattern of movement precursor of the failure on the European Alps, for landslide characteristics  $\alpha = 1.5$  and  $A = 0.052$ . The Harmalière site study is located with a black dot. The general topography is shown as isocontours spaced every 500 m.

### 5.2. Detection ability of the Sentinel-2 satellite

In this section, the question is raised about the representativity of the Harmalière case study, that is whether this precursor detection was completely fortunate or if detecting motions prior to landslide failures is a real potential of the Sentinel-2 constellation. To generalize the observations made on the Harmalière landslide, we simulate the probability to detect a motion precursory to landslide failure with Sentinel-2. This simulation is conducted as a function of its revisit time  $R$ , in an ideal case where the landslide movement is following a classical Voight's law (Fukuzono, 1985; Voight, 1989) toward the failure, regardless of its deformation mechanism and type of material. This former law links the acceleration ( $\ddot{D}$ ) and the velocity ( $\dot{D}$ ) of a creeping material toward failure:

$$\ddot{D} = A\dot{D}^\alpha \quad (1)$$

where  $A$  and  $\alpha$  are characteristics of the landslide material. Typical values of  $\alpha$  are close to 1.5 (Federico et al., 2012) but with possible large variability between 1.1 and 2.2 (Crosta and Agliardi, 2003). Federico et al. (2012) also provide values for  $A$  around 0.05. These values control the motion of the moving mass close to its rupture. Larger  $\alpha$  and  $A$  values lead to shorter time-scales of acceleration. Although many landslides can be described by this law (Federico et al., 2012), some others exhibit more complex behaviour toward failure, due to specific geometries of basal sliding surfaces or to specific forcings (rainfalls for instance) (e.g. Petley et al., 2002). We do not aim at simulating this complexity.

Integrating Eq. (1) for  $A \geq 0$  and  $\alpha \geq 1$ , one obtains

$$\dot{D} = [A(\alpha - 1)(t_f - t)]^{-1/(\alpha-1)} \quad (2)$$

where  $t$  is the time before the failure time  $t_f$ . The displacement between 2 successive satellite cloud-free acquisitions at time  $T$  and  $T + \Delta t$ , is then given by

$$D = \int_T^{T+\Delta t} \dot{D} dt \quad (3)$$

We calculate the probability to detect a motion prior to the landslide failure using Sentinel-2 constellation (both satellites A and B), that is we calculate the probability that a measured displacement over a time period  $[T, T + \Delta t]$  before the landslide rupture is greater than the Sentinel-2 measurements uncertainty  $\sigma$  (here 1.59 m, see Section 4.1). In our case,  $\Delta t$  is a multiple of the revisit time  $R$ . Let us denote  $N + 1$  the number of images acquired at times  $[T, T + R, T + 2R, \dots, T + N \cdot R]$ , where  $T + N \cdot R < t_f$ . These images can either be cloud-free (value 1) or cloudy (value 0). Let  $E$  be the event that the displacement between 2 cloud-free images acquired before the failure is greater than  $\sigma$ , assigned with a probability  $P(E)$ . Since the motion (displacement and velocity) given by Voight's law is an increasing function of time, the calculation of  $P(E)$  reduces to the probability that the displacement measured between the 2 last cloud-free acquisitions before failure is greater than  $\sigma$ .

As an example, using  $N = 4$ , the combinations that meet the defined criteria of only 2 successive cloud-free acquisitions are

$$\text{Combination}_{N=4} = \begin{bmatrix} 1, 1, 0, 0, 0 \\ 1, 0, 1, 0, 0 \\ 1, 0, 0, 1, 0 \\ 1, 0, 0, 0, 1 \end{bmatrix} \quad (4)$$

The probability  $P(C_2^N)$  that one of these sequences is realized, is a function of the probability  $P(C)$  that a given image is cloud-free:

$$P(C_2^N) = N \cdot P(C)^2 \cdot (1 - P(C))^{N-1} \quad (5)$$

$P(E)$  can then be formulated as follows:

$$P(E) = \sum_{N=1}^{N=\infty} P(E|C_2^N) P(C_2^N) \quad (6)$$

Using Eq. (3), we can calculate numerically the displacement between two acquisitions at two given time before failure, and thus the



number of acquisition pairs that meet the criteria of displacement greater than  $\sigma$ , which conducts to the probability  $P(E|C_2^N)$  to have a displacement greater than  $\sigma$  for two given acquisitions before  $t_f$ . Combining Eqs. (6) and (5) gives the following:

$$P(E) = \sum_{N=1}^{N=\infty} P(E|C_2^N) N \cdot P(C)^{2N} (1 - P(C))^{N-1} \quad (7)$$

This summation over  $N$  converges rapidly, so that we limit the numerical integration until  $N = 20$ .

$P(E)$  is only dependent on  $(R, \alpha$  and  $P(C))$ . It is represented in Fig. 6 as a function of these 3 parameters. The revisit time  $R$  is a function of the number of available satellites orbits ( $N_{orbit}$ ) per unit of time, which depends on the geographic location of the observed area (Kaab et al., 2016).

Taking typical  $\alpha$  and  $A$  values of 1.5 and 0.052 respectively (e.g. Federico et al., 2012), the probability to detect accelerating landslides in an area covered half time by clouds with 1 image every 5 days is 55%, increasing to 97% in areas where the satellites provide a daily cover.

We use the relation of Eq. (7), together with a global cloud cover map (Wilson and Jetz, 2016), derived from 15 years of cloud measurements at the kilometeric scale, and the global Sentinel-2 swath coverage (Kaab et al., 2016) to derive a realistic revisit time  $R$ , and then a global map up to 83° latitudes (Li and Roy, 2017) for probabilistic detection of landslide precursors (see Eq. (7)). These maps are derived for  $\alpha = 1.5$  and 1.7 in Figs. 7 and 8 respectively. A zoom on the European Alps is provided in Fig. 9 for  $\alpha = 1.5$ . It should be noted, that for polar regions, our simulation does not take into account the seasonal variation of illumination, that prevents to acquire optical images during winter time. The probabilities are therefore smoothed over the year.

We first see that the probability to detect a precursory motion before failure is very heterogeneous spatially, both at the global scale and over short distances. This variability is firstly explained by the theoretical number of available satellite tracks, which varies by a factor of up to 8 from 0° to 83° latitude (Figs. 7 and 8), but also may vary by a factor of 3 over short distances (Fig. 9). This variability is secondly explained by the daily cloud cover that varies between 0.7% and 85% for 99% of the globe, diminishing the number of available tracks compared to the theoretical one.

Using a typical value for  $\alpha$  of 1.5 leads to detection probability of between 20% and 100% in the European Alps. The calculated probability to have one cloud-free image over a landslide based on this dataset is certainly a little too low. Indeed, the global daily cloud cover slightly over-estimates the in situ measurements (Wilson and Jetz, 2016), and the daily cloud cover corresponds to the probability to have one cloud per day on a 1 km<sup>2</sup> pixel. Over the Harmalière area, the global dataset and the available Sentinel-2 data actually match well, with 54% of cloud probability in the global dataset, and 56% of images unexploitable due to too much cloud cover.

Furthermore, all those values are also a function of the image correlation uncertainties which can vary from one area to another due to differences of vegetation covers (e.g. Delacourt et al., 2004; Stumpf et al., 2014; Lacroix et al., 2015). On the Harmalière landslide, vegetation varied very quickly during the studied period, so that the 1.59 m of mean uncertainty can be considered as a relatively conservative value. Consequently, results with lower uncertainty are expected in areas with lower vegetation cover.

Finally, the probability of detection is strongly affected by parameter  $\alpha$ , which relates to the evolution of the landslide kinematics toward the failure (Figs. 7 and 8). For instance, on the Harmalière area the probability to detect a landslide precursor is 14%, 65% and, 100% for  $\alpha = 1.7$ , 1.5 and 1.3, respectively. This highlights the need to better characterize the behaviour of landslides toward the failure. Most of the studies (e.g. Federico et al., 2012) found a value of  $\alpha$  close to 1.5, so that the map of Fig. 7 can be considered as the average probability. Local

variations due to differences in geological settings are however expected. For  $\alpha$  larger than 1.8, corresponding to landslides with slow velocities at the failure, the last stage of creep cannot be detected by Sentinel-2 images. InSAR measurements may be better appropriate for this detection, despite limitations of the method due to relief shadows and vegetation (Dong et al., 2018; Intrieri et al., 2018). In contrast, the probability to detect landslides with high velocity prior to the failure ( $\alpha \leq 1.4$ ) reaches 100%. This shows that the detection of the Harmalière precursory pattern is not a fortunate case and that Sentinel-2 images have a large value for this pre-failure detection.

## 6. Conclusions

The analysis of Sentinel-2 images over an area affected by active landslides as well as simulations of Sentinel-2 acquisitions over typical creeping landslides show that these free and global satellite images are able to detect transient motions of large landslides, thanks to their frequent revisit time. This detection is however limited to large landslides, due to the medium resolution of these satellites. As these motions can be precursors to landslide failures, medium resolution optical satellite constellations open a wide area of research for the understanding of landslide mechanism and for the development of early warning systems. Furthermore, the combination of the Sentinel-2 constellation together with the existing 15 m resolution Landsat-7/8 constellation, provides now a 3-day revisit time at the Equator, opening exciting opportunities for landslide monitoring. Our study suggests that comparing images with different orbits leads to a slight increase in uncertainties but at the same time makes the image correlation sensitive to vertical motions that can be prominent at the landslide headscarps. This conclusion should drive the strategy for time-series correlation from different satellites, for instance Sentinel-2 and Landsat-7/8 data. In the same time, the processing of large amounts of data opens the era of time-series analysis, with the possibility to decrease the uncertainty using the redundancy of the measurements. Several approaches have recently been implemented on glaciers (Dehecq et al., 2015; Fahnestock et al., 2015) using Landsat-8 data, and future developments should benefit also to both glacier and solid-earth communities.

## Acknowledgments

This study benefited from discussions with J.R. Grasso. The authors also thank the support from ESA through the Alcantara project “Monitoring and Detection of Landslides from optical Images time-Series” (ESA 15/P26). This work has been supported by a grant from Labex OSUG@2020 (Investissements d’avenir ANR10 LABEX56). The Sentinel-2 data can be accessed freely on the Sentinels Scientific Data Hub.

## References

- Al Hayari, M., Antoine, P., Biguenet, G., Monnet, J., Mora, H., 1990. Détermination des caractéristiques mécaniques au cisaillement des argiles litées. Cas du glissement de la combe d’harmalière. *Rev. Fr. Géotech.* 50, 71–77.
- Altena, B., Kaab, A., 2017. Elevation change and improved velocity retrieval using orthorectified optical satellite data from different orbits. *Remote Sens.* 9 (3), 300.
- Amirano, D., Grasso, J.R., Senfaute, G., 2005. Seismic precursory patterns before a cliff collapse and critical point phenomena. *Geophys. Res. Lett.* 32, 5. <http://dx.doi.org/10.1029/2004GL022270>.
- Bennett, G.L., Roering, J.J., Mackey, B.H., Handwerger, A.L., Schmidt, D.A., Guillod, B.P., 2016. Historic drought puts the brakes on earthflows in northern California. *Geophys. Res. Lett.* 43. <http://dx.doi.org/10.1002/2016GL068378>.
- Berardino, P., Fornaro, G., Lanari, R., Sansosti, E., 2002. A new algorithm for surface deformation monitoring based on small baseline differential SAR interferograms. *IEEE Trans. Geosci. Remote Sens.* 40 (11), 2375–2383.
- Berthier, E., Vadon, H., Baratoux, D., Arnaud, Y., Vincent, C., Feigl, K., Rémy, F., Legrésy, B., 2005. Surface motion of mountain glaciers derived from satellite optical imagery. *Remote Sens. Environ.* 95 (1), 14–28. <http://dx.doi.org/10.1016/j.rse.2004.11.005>.
- Bhandari, R., 1988. Special lecture: Some practical lessons in the investigation and field monitoring of landslides. In: Bonnard (Ed.), *Proceedings of the Fifth International Symposium on Landslides, Lausanne*. v.3. A.A. Balkema, Rotterdam, pp. 1435–1457.

- Bièvre, G., Jongmans, D., Winiarski, T., Zumbo, V., 2012. Application of geophysical measurements for assessing the role of fissures in water infiltration within a clay landslide (Trièves area, French Alps). *Hydrol. Process.* 26 (14), 2128–2142. <http://dx.doi.org/10.1002/hyp.7986>.
- Bièvre, G., Knief, U., Jongmans, D., Pathier, E., Schwartz, S., van Westen, C.J., Villemin, T., Zumbo, Z., 2011. Paleotopographic control of landslides in lacustrine deposits (Trièves plateau, French western Alps). *Geomorphology* 125 (1), 214–224. <http://dx.doi.org/10.1016/j.geomorph.2010.09.018>.
- Bontemps, N., Lacroix, P., Doin, M., 2018. Inversion of deformation fields time-series from optical images, and application to the long term kinematics of slow-moving landslides in Peru. *Remote Sens. Environ.* 210, 144–158. <http://dx.doi.org/10.1016/j.rse.2018.02.023>.
- Calabro, M., Schmidt, D., Roering, J., 2010. An examination of seasonal deformation at the Portuguese bend landslide, southern California, using radar interferometry. *J. Geophys. Res.* 115 (F2).
- Crosta, G.B., Agliardi, F., 2003. Failure forecast for large rock slides by surface displacement measurements. *Can. Geotech. J.* 191 (1), 176–191. <http://dx.doi.org/10.1139/T02-085>.
- Debella-Gilo, M., Kaab, A., 2012. Measurement of surface displacement and deformation of mass movements using least squares matching of repeat high resolution satellite and aerial images. *Remote Sens.* 4 (1), 43–67.
- Dehecq, A., Gournelen, N., Trouve, E., 2015. Deriving large-scale glacier velocities from a complete satellite archive: application to the Pamir-Karakoram-Himalaya. *Remote Sens. Environ.* 162, 55–66. <http://dx.doi.org/10.1016/j.rse.2015.01.031>.
- Delacourt, C., Allemand, P., Casson, B., Vadon, H., 2004. Velocity field of the La Clapière landslide measured by the correlation of aerial and QuickBird satellite images. *Geophys. Res. Lett.* 31 (15). <http://dx.doi.org/10.1029/2004GL020193>. N/a-n/a.
- Dong, J., Zhang, L., Li, M., Yu, Y., Liao, M., Gong, J., Luo, H., 2018. Measuring precursory movements of the recent Xinmo landslide in Mao County, China with Sentinel-1 and ALOS-2 PALSAR-2 datasets. *Landslides* 15 (1), 135–144.
- Drusch, M., Bello, U.D.e.l., Carlier, S., Colin, O., Fernandez, V., Gascon, F., Hoersch, B., Isola, C., Laberinti, P., Martimort, P., Meygret, A., Spoto, F., Sy, O., Marchese, F., Bargellini, P., 2012. Sentinel-2: ESA's optical high-resolution mission for GMES operational requirements. *Remote Sens. Environ.* 120, 25–36. <http://dx.doi.org/10.1016/j.rse.2011.11.026>.
- Fahnestock, M., Scambos, T., Moon, T., Gardner, A., Haran, T., Klinger, M., 2015. Rapid large-area mapping of ice flow using Landsat 8. *Remote Sens. Environ.* <http://dx.doi.org/10.1016/j.rse.2015.11.023>.
- Federico, A., Popescu, M., Elia, G., Fidelibus, C., Internò, G., Murianni, A., 2012. Prediction of time to slope failure: a general framework. *Environ. Earth Sci.* 66 (1), 245–256. <http://dx.doi.org/10.1007/s12665-011-1231-5>.
- Fernandez, P., Whitworth, M., 2016. A new technique for the detection of large scale landslides in glacio-lacustrine deposits using image correlation based upon aerial imagery: a case study from the French Alps. *Int. J. Appl. Earth Obs. Geoinf.* 52, 1–11. <http://dx.doi.org/10.1016/j.jag.2016.05.002>.
- Fukuzono, T., 1985. A new method for predicting the failure time of a slope. In: *Proceedings of 4th International Conference and Field Workshop on Landslides*, Tokyo, pp. 145–150.
- Giraud, A., Antoine, P., Van Asch, T.W.J., Nieuwenhuis, J.D., 1991. Geotechnical problems caused by glaciolacustrine clays in the French Alps. *Eng. Geol.* 31, 185–195. [http://dx.doi.org/10.1016/0013-7952\(91\)90005-6](http://dx.doi.org/10.1016/0013-7952(91)90005-6).
- Hendron, A.J., Patton, F.D., 1985. The Vaiont Slide, a geotechnical analysis based on how geologic observations of the failure surface. U.S. Army Corps of Engineers. In: *Technical Report 85. number 5*. pp. 104.
- Hilley, G., Burgmann, R., Ferretti, A., Novali, F., Rocca, F., 2004. Dynamics of slow-moving landslides from permanent scatterer analysis. *Science* 304 (5679), 1952–1955.
- Hungr, O., Leroueil, S., Picarelli, L., 2014. The Varnes classification of landslide types, an update. *Landslides* 11 (2), 167–194. <http://dx.doi.org/10.1007/s10346-013-0436-y>.
- Intrieri, E., Raspini, F., Fumagalli, A., Lu, P., Del Conte, S., Farina, P., Allievi, J., Ferretti, A., Casagli, N., 2018. The Maoxian landslide as seen from space: detecting precursors of failure with Sentinel-1 data. *Landslides* 15 (1), 123–133.
- Iverson, R.M., 2000. Landslide triggering by rain infiltration. *Water Resour. Res.* 36 (7), 1897–1910. <http://dx.doi.org/10.1029/2000WR900090>.
- Jongmans, D., Bièvre, G., Schwartz, S., Renalier, F., Bearez, N., 2009. Geophysical investigation of the large avignonet landslide in glaciolacustrine clays in the Trièves area (French Alps). *Eng. Geol.* 109, 45–56. <http://dx.doi.org/10.1016/j.enggeo.2008.10.005>.
- Kaab, A., Winsvold, S.H., Altena, B., Nuth, C., Nagler, T., Wuite, J., 2016. Glacier remote sensing using sentinel-2. Part I: radiometric and geometric performance, and application to ice velocity. *Remote Sens.* 8 (598). <http://dx.doi.org/10.3390/rs8070598>.
- Knief, U., 2011. Quantification of Clayey Landslides Evolution From Remote Sensing Techniques: Application to the Trièves Area (French Alps). PhD Thesis. Université de Grenoble, France.
- Kos, A., Amann, F., Strozzi, T., Delaloye, R., von Ruette, J., Springman, S., 2016. Contemporary glacier retreat triggers a rapid landslide response, Great Aletsch Glacier, Switzerland. *Geophys. Res. Lett.* 43 (24), 466–474.
- Lacroix, P., Amitrano, D., 2013. Long-term dynamics of rockslides and damage propagation inferred from mechanical modeling. *J. Geophys. Res. Earth Surf.* 118 (4), 2292–2307. <http://dx.doi.org/10.1002/2013JF002766>.
- Lacroix, P., Berthier, E., Maquerhua, E.T., 2015. Earthquake-driven acceleration of slow-moving landslides in the Colca Valley, Peru, detected from Pléiades images. *Remote Sens. Environ.* 165, 148–158. <http://dx.doi.org/10.1016/j.rse.2015.05.010>.
- Lacroix, P., Perfettini, H., Taipei, E., Guiller, B., 2014. Co- and postseismic motion of a landslide; observations, modelling and analogy with tectonic faults. *Geophys. Res. Lett.* <http://dx.doi.org/10.1002/2014GL061170>. pp. n/a-n/a.
- Lacroix, P., Zavala, B., Berthier, E., Audin, L., 2013. Supervised method of landslide inventory using panchromatic SPOT5 images and application to the earthquake-triggered landslides of Pisco (Peru, 2007, Mw8.0). *Remote Sens.* 5 (6), 2590–2616. <http://dx.doi.org/10.3390/rs5062590>.
- Leprince, S., Barbot, S., Ayoub, F., Avouac, J.P., 2007. Automatic and precise orthorectification, coregistration, and subpixel correlation of satellite images, application to ground deformation measurements. *IEEE Trans. Geosci. Remote Sens.* 45 (6), 1529–1558. <http://dx.doi.org/10.1109/TGRS.2006.888937>.
- Li, J., Roy, D.P., 2017. A global analysis of Sentinel-2A, Sentinel-2B and landsat-8 data revisit intervals and implications for terrestrial monitoring. *Remote Sens.* 9 (9), 902.
- Mainsant, G., Jongmans, D., Chambon, G., Larose, E., Baillet, L., 2012a. Shear-wave velocity as an indicator for rheological changes in clay materials: lessons from laboratory experiments. *Geophys. Res. Lett.* 39 (19). <http://dx.doi.org/10.1029/2012GL053159>.
- Mainsant, G., Larose, E., Brönnimann, C., Jongmans, D., Michoud, C., Jaboyedoff, M., 2012b. Ambient seismic noise monitoring of a clay landslide: toward failure prediction. *J. Geophys. Res.* 117, F01030.
- Moulin, C., Robert, Y., 2004. Le glissement de l'harmalière sur la commune de sinard. In: *Proceedings of the Workshop Ryskyhydrogeol, Program Interreg III, La Mure (France)*, pp. 11.
- Petley, D.N., Bulmer, M.H., Murphy, W., 2002. Patterns of movement in rotational and translational landslides. *Geology* 30 (8), 719–722. [http://dx.doi.org/10.1130/0091-7613\(2002\)030<0719:POMIRA>2.0.CO;2](http://dx.doi.org/10.1130/0091-7613(2002)030<0719:POMIRA>2.0.CO;2).
- Renalier, F., Jongmans, D., Campillo, M., Bard, P.Y., 2010a. Shear wave velocity imaging of the Avignonet landslide (France) using ambient noise cross-correlation. *J. Geophys. Res.* 115, F03032. <http://dx.doi.org/10.1029/2009JF001538>.
- Renalier, F., Bièvre, G., Jongmans, D., Campillo, M., Bard, P.Y., 2010b. Characterization and monitoring of unstable clay slopes using active and passive shear wave velocity measurements. In: *Miller, R.D., Bradford, J.D., Holliger, K. (Eds.), Advances in Near-Surface Seismology and Ground-Penetrating Radar, Geophysical Developments Series N. 15. Society of Exploration Geophysics, Tulsa, USA*, pp. 397–414.
- French multidisciplinary observatory of versant instabilities. In: *RESIF - Réseau Sismologique et géodésique Français*, <http://dx.doi.org/10.15778/RESIF.MT>.
- Roering, J.J., Stimely, L.L., Mackey, B.H., Schmidt, D.A., 2009. Using DInSAR, airborne LiDAR, and archival air photos to quantify landsliding and sediment transport. *Geophys. Res. Lett.* 36, L19402. <http://dx.doi.org/10.1029/2009GL040374>.
- Strozzi, T., Delaloye, R., Kaab, A., Ambrosi, C., Perruchoud, E., Wegmüller, U., 2010. Combined observations of rock mass movements using satellite SAR interferometry, differential GPS, airborne digital photogrammetry, and airborne photography interpretation. *J. Geophys. Res.* 115. <http://dx.doi.org/10.1029/2009JF001311>.
- Stumpf, A., Malet, J.P., Allemand, P., Ulrich, P., 2014. Surface reconstruction and landslide displacement measurements with Pléiades satellite images. *ISPRS J. Photogramm. Remote Sens.* 95, 1–12. <http://dx.doi.org/10.1016/j.isprsjprs.2014.05.008>.
- Stumpf, A., Malet, J.P., Delacourt, C., 2017. Correlation of satellite image time-series for the detection and monitoring of slow-moving landslides. *Remote Sens. Environ.* 189, 40–55.
- Sun, Q., Zhang, L., Ding, X., Hu, J., Li, Z., Zhu, J., 2015. Slope deformation prior to Zhouqu, China landslide from InSAR time series analysis. *Remote Sens. Environ.* 156, 45–57. <http://dx.doi.org/10.1016/j.rse.2014.09.029>.
- Van Asch, T.W.J., Brinkhorst, W.H., Buist, H.J., Vessem, P.V., 1984. The development of landslides by retrogressive failure in varved clays. *Z. Geomorphol. Suppl.* 4, 165–181.
- Van Asch, T.W.J., Malet, J.P., Bogaard, T.A., 2009. The effect of groundwater fluctuations on the velocity pattern of slow-moving landslides. *Nat. Hazards Earth Syst. Sci.* 9 (3), 739–749.
- Van Genuchten, P.M.B., Van Asch, T.W.J., 1988. Factors controlling the movement of a landslide in varved clays near La Mure (French Alps). *Bull. Soc. Geol. Fr.* 8 (3), 461–469.
- Voight, B., 1989. A relation to describe rate-dependent material failure. *Science* 243 (4888), 200–203. <http://dx.doi.org/10.1126/science.243.4888.200>.
- Wilson, A.M., Jetz, W., 2016. Remotely sensed high-resolution global cloud dynamics for predicting ecosystem and biodiversity distributions. *PLoS Biol* 14 (3). <http://dx.doi.org/10.1371/journal.pbio.1002415>.
- Zerathe, S., Lacroix, P., Jongmans, D., Marino, J., Taipei, E., Wathelet, M., Pari, W., Smoll, L.F., Norabuena, E., Guiller, B., Tatar, L., 2016. Morphology, structure and kinematics of a rainfall controlled slow-moving Andean landslide, Peru: the Maca slow-moving Andean landslide. *Earth Surf. Process. Landf.* 41 (11), 1477–1493. <http://dx.doi.org/10.1002/esp.3913>.
- Zvebil, J., Moser, M., 2001. Monitoring based time-prediction of rock falls: three case-histories. *Phys. Chem. Earth Part B* 26 (2), 159–167. [http://dx.doi.org/10.1016/S1464-1909\(00\)00234-3](http://dx.doi.org/10.1016/S1464-1909(00)00234-3).